

Brain MRI Segmentation with Fast and Globally Convex Multiphase Active Contours

Juan C. Moreno*, V. B. S. Prasath[†], Hugo Proença[‡], K. Palaniappan[§]

Abstract

Multiphase active contour based models are useful in identifying multiple regions with different characteristics such as the mean values of regions. This is relevant in brain magnetic resonance images (MRIs), allowing the differentiation of white matter against gray matter. We consider a well defined globally convex formulation of Vese and Chan multiphase active contour model for segmenting brain MRI images. A well-established theory and an efficient dual minimization scheme are thoroughly described which guarantees optimal solutions and provides stable segmentations. Moreover, under the dual minimization implementation our model perfectly describes disjoint regions by avoiding local minima solutions. Experimental results indicate that the proposed approach provides better accuracy than other related multiphase active contour algorithms even under severe noise, intensity inhomogeneities, and partial volume effects.

Keywords: Image segmentation, active contours, multiphase, globally convex, dual formulation, brain MRI.

1 Introduction

The aim of image segmentation is to obtain meaningful partitions of an input image into a finite number of disjoint homogeneous objects. Active contour models are popular in the regard. Chan and Vese [20] proposed an active contour without edges scheme based on the classical work of Mumford and Shah [40] variational energy minimization model. Since biomedical images typically have multiple regions of interest with different characteristics, deriving a multiphase active contour scheme for efficient segmentation is an important area of research in image processing [19, 48, 31].

*Corresponding author. IT, Department of Computer Science, University of Beira Interior, 6201-001, Portugal E-mail: jmoreno@ubi.pt

[†]Department of Computer Science, University of Missouri-Columbia, MO 65211 USA. E-mail: prasaths@missouri.edu

[‡]IT, Department of Computer Science, University of Beira Interior, 6201-001, Portugal. E-mail: hugomcp@ubi.pt

[§]Department of Computer Science, University of Missouri-Columbia, MO 65211 USA. E-mail: palaniappan@missouri.edu

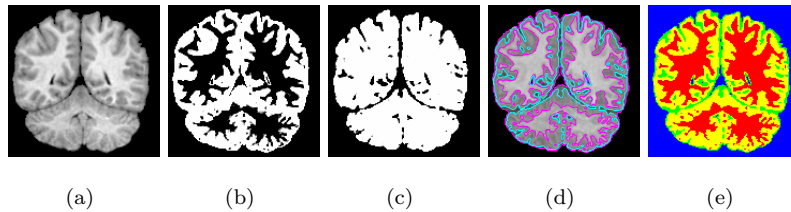


Figure 1: Our fast and automatic four phase image segmentation scheme provides a better segmentations for brain MRI images, it differentiates the gray matter from the surrounding white region clearly. (a) Input image with noise level $n = 5\%$, (b) & (c) show final binary segmentations obtained by thresholding the relaxed functions u_1, u_2 at 0.5, (d) final segmentation result showing the contours superimposed on the input image, (e) color coded visualization of the obtained segmentation result.

In MRI (magnetic resonance image) images, segmentations based on active contours have been used with traditional level set method [41]. Active contours can also be improved using region information [24], salient features [32] or mathematical morphology [29] etc. Traditionally these schemes use a gradient descent formulation to implement the non-convex energy minimization and can stuck in undesired local minima thereby lead to erroneous segmentations. Moreover, traditional level set based implementation is prone to slower convergence due to the well-known re-initialization requirement and discretization errors. More recently quite a lot of interest is being shown in techniques that can obtain a general convex formulation for active contours schemes based on energy minimization which can alleviate the problem of local minima at the same time focussing on the computational complexity [23, 13, 8, 14, 39, 30]. Among other techniques for MRI image segmentation, we mention fuzzy C-means based models [1, 35, 21], fuzzy connectedness [52], automatic labeling [27], adaptive expectation-maximization (EM) [49], Bayesian EM [37], hidden Markov model EM [51], kernel clustering [34], optimum-path clustering [15], anisotropic diffusion combined with classical snakes model [3], discriminant analysis [2], and neural networks [46]. We also refer to [42, 43, 36] for reviews about segmentation for medical images in general and [11] for MR images in particular. The area of MRI image segmentation has seen tremendous research activity and a more detailed review in this particular field can be found in [9].

In this paper, we consider a globally convex version of the four phase piecewise constant energy functional following the seminal work of Chan et al [18]. By deriving an approximate novel convex functional we change the original formulation into a binary segmentation problem and utilize a dual minimization to solve the relaxed formulation [16]. The proposed global methodology avoids the level set re-initialization constraint and other ad-hoc techniques [38] used for fixing level set active contour movements throughout the iterations. The proposed approach is used to obtain white matter and gray matter partitions on brain MRI images as can be seen for example in Figure 1. Our scheme does not involve level sets or re-initialization and instead relies on the relaxed globally convex formulation of the Vese and Chan multiphase active contours. Comparison results on the different image sets with varying

noise and inhomogeneities show that we can obtain better results than traditional level set multiphase schemes [48, 5, 7, 6, 10] and primal-dual approach of [17]. Moreover, compared to these traditional level set based implementations we achieve faster convergence due to the usage of efficient alternating dual minimization. The proposed approach is general in the sense that we can add domain specific knowledge to improve such active contour schemes further for various tasks [33, 50, 26, 25, 44, 45].

The main contribution of our work is two-fold: 1) a fast four phase active contour model using a relaxed globally convex minimization approximation; 2) using an efficient dual minimization based implementation for performing segmentation on MRI images. The rest of the paper is organized as follows. Section 2 introduces the multiphase variational active contour scheme and provides a globally convex formulation. Section 3 illustrates the segmentation results on various Brain MRI images including comparison of different schemes. Finally, Section 4 concludes the paper.

2 Multiphase active contours model

We first recall the multiphase formulation of Vese and Chan [48] and restrict ourselves to the piecewise constant four phase model since the general case can be derived similarly. Let $\phi_1, \phi_2 : \Omega \subset \mathbb{R}^2 \rightarrow \mathbb{R}$ be the two level sets. $H_1 = H(\phi_1)$, $H_2 = H(\phi_2)$ and $\tilde{H}_1 = 1 - H(\phi_1)$, $\tilde{H}_2 = 1 - H(\phi_2)$, where H is the Heaviside function, representing four regions. Our goal is to solve a minimization problem

$$\min_{(\mathbf{c}, \Phi)} F(\mathbf{c}, \Phi) \quad (1)$$

with

$$\begin{aligned} F(\mathbf{c}, \Phi) &= \mu_1 \int_{\Omega} \delta(\phi_1) |\nabla \phi_1| d\mathbf{x} + \mu_2 \int_{\Omega} \delta(\phi_2) |\nabla \phi_2| d\mathbf{x} \\ &+ \lambda_{11} \int_{\Omega} (I - c_{11})^2 H_1 H_2 d\mathbf{x} + \lambda_{10} \int_{\Omega} (I - c_{10})^2 H_1 \tilde{H}_2 d\mathbf{x} \\ &+ \lambda_{01} \int_{\Omega} (I - c_{01})^2 \tilde{H}_1 H_2 d\mathbf{x} + \lambda_{00} \int_{\Omega} (I - c_{00})^2 \tilde{H}_1 \tilde{H}_2 d\mathbf{x} \end{aligned}$$

where $\Phi = (\phi_1, \phi_2)$, and the constant mean values $\mathbf{c} = (c_{11}, c_{10}, c_{01}, c_{00})$ can be derived as

$$\begin{aligned} c_{11} &= \frac{\int_{\Omega} I H_1 H_2 d\mathbf{x}}{\int_{\Omega} H_1 H_2 d\mathbf{x}}, & c_{10} &= \frac{\int_{\Omega} I H_1 \tilde{H}_2 d\mathbf{x}}{\int_{\Omega} H_1 \tilde{H}_2 d\mathbf{x}} \\ c_{01} &= \frac{\int_{\Omega} I \tilde{H}_1 H_2 d\mathbf{x}}{\int_{\Omega} \tilde{H}_1 H_2 d\mathbf{x}}, & c_{00} &= \frac{\int_{\Omega} I \tilde{H}_1 \tilde{H}_2 d\mathbf{x}}{\int_{\Omega} \tilde{H}_1 \tilde{H}_2 d\mathbf{x}} \end{aligned}$$

Note the the zero level sets $\phi_i = 0$, $i = 1, 2$, represent object boundaries and the mean values \mathbf{c} represent the expected average pixel values in these objects. Vese and Chan [48] used the corresponding gradient descent equations to implement the active contours [41]. In the numerical implementation of the above PDEs, a non-compactly supported, smooth approximation of the Heaviside function $H_{\epsilon}(\mathbf{x})$, such that $H_{\epsilon}(\mathbf{x}) \rightarrow H(\mathbf{x})$ as $\epsilon \rightarrow 0$ is utilized. Since the above minimization (1) is non-convex the time discretized

gradient descent PDEs usually require large iterations and small time steps to convergence (typically in 100's of iterations). Moreover, the final segmentation result may not correspond to the global minimum of the energy function as the gradient descent scheme can be stuck at a local minima of the corresponding energy functional given in Eqn. (1).

We briefly recall the corresponding gradient descent equations (time dependent Euler-Lagrange equations of Eqn. (1)) for the level sets functions ϕ_1 and ϕ_2 ,

$$\phi_{1t} = \delta(\phi_1) \left(\mu_1 \operatorname{div} \left(\frac{\nabla \phi_1}{|\nabla \phi_1|} \right) - r_1(\mathbf{c}, H_2) \right) \quad (2)$$

and

$$\phi_{2t} = \delta(\phi_2) \left(\mu_2 \operatorname{div} \left(\frac{\nabla \phi_2}{|\nabla \phi_2|} \right) - r_2(\mathbf{c}, H_1) \right) \quad (3)$$

respectively. Here, the image fitting terms are given by,

$$\begin{aligned} r_1(\mathbf{c}, H_2) &= (\lambda_{11}(I - c_{11})^2 - \lambda_{01}(I - c_{01})^2)H_2 \\ &\quad + (\lambda_{10}(I - c_{10})^2 - \lambda_{00}(I - c_{00})^2)\tilde{H}_2 \\ r_2(\mathbf{c}, H_1) &= (\lambda_{11}(I - c_{11})^2 - \lambda_{10}(I - c_{10})^2)H_1 \\ &\quad + (\lambda_{01}(I - c_{01})^2 - \lambda_{00}(I - c_{00})^2)\tilde{H}_1. \end{aligned}$$

Following, Chan et al [18], we derive a relaxed energy minimization formulation by dropping the dirac delta function ($\delta(\phi)$ in (2) and (3)) to obtain,

$$\min_{(\Phi, \mathbf{c})} \mathcal{F}(\Phi, \mathbf{c}) \quad (4)$$

with

$$\mathcal{F}(\mathbf{c}, \Phi) = \mu_1 \int_{\Omega} |\nabla \phi_1| d\mathbf{x} + \mu_2 \int_{\Omega} |\nabla \phi_2| d\mathbf{x} + \int_{\Omega} r_1(\mathbf{c}, H_2)\phi_1 + \int_{\Omega} r_2(\mathbf{c}, H_1)\phi_2 d\mathbf{x}$$

Then correspondingly we can derive an energy functional which does not depend on regularized Heaviside functions. Thus, we can solve the following globally convex energy minimization problem,

$$\min_{\mathbf{u}=(u_1, u_2) \in \{0,1\}^2} \mathcal{G}(\mathbf{c}, \mathbf{u}) \quad (5)$$

with

$$\begin{aligned} \mathcal{G}(\mathbf{c}, \mathbf{u}) &= \mu_1 \int_{\Omega} |\nabla u_1| d\mathbf{x} + \mu_2 \int_{\Omega} |\nabla u_2| d\mathbf{x} \\ &\quad + \lambda_{11} \int_{\Omega} (I - c_{11})^2 u_1 u_2 d\mathbf{x} + \lambda_{01} \int_{\Omega} (I - c_{01})^2 (1 - u_1) u_2 d\mathbf{x} \\ &\quad + \lambda_{10} \int_{\Omega} (I - c_{10})^2 u_1 (1 - u_2) d\mathbf{x} + \lambda_{00} \int_{\Omega} (I - c_{00})^2 (1 - u_1) (1 - u_2) d\mathbf{x}, \end{aligned}$$

where Heaviside functions are replaced by $\mathbf{u} = (u_1, u_2) \in \{0, 1\}^2$ which are known as *binary partitioning functions*. The above modified minimization problem (5) can further be relaxed to the set of functions

$\mathbf{u} = (u_1, u_2) \in [0, 1]^2$ in order to solve a convex minimization problem. That is, the binary partitioning functions based energy minimization becomes,

$$\min_{\mathbf{u}=(u_1, u_2) \in [0, 1]^2} \mathcal{G}(\mathbf{c}, \mathbf{u}). \quad (6)$$

The following theorem provides the guarantee of finding a global minimizer for the derived functional (5) in terms of the relaxed version in (6). We follow arguments similar to the work of Chan et al [18] and [39] to prove the following result.

Theorem 1. *For any $c_{11}, c_{10}, c_{01}, c_{00} \in \mathbb{R}$, a global minimizer for $\mathcal{G}(\mathbf{c}, \cdot)$ in (5) can be found by carrying out the convex minimization problem (6).*

Proof. We use the standard notation for functions of bounded variation [4]. Since $\mathbf{u} \in [0, 1]^2$, it follows from the standard total variation based Coarea Formula,

$$\int_{\Omega} |\nabla u_1| d\mathbf{x} = \int_0^1 \int_0^1 \text{Per}(\{\mathbf{x} \in \Omega : u_1(\mathbf{x}) > \zeta_1\}; \Omega) d\zeta_1 d\zeta_2$$

and

$$\int_{\Omega} |\nabla u_2| d\mathbf{x} = \int_0^1 \int_0^1 \text{Per}(\{\mathbf{x} \in \Omega : u_2(\mathbf{x}) > \zeta_2\}; \Omega) d\zeta_1 d\zeta_2.$$

For the image fitting term,

$$\begin{aligned} \int_{\Omega} (u - c_{11})^2 u_1 u_2 d\mathbf{x} &= \int_{\Omega} (u - c_{11})^2 \prod_{i=1}^2 \left(\int_0^1 \mathbb{1}_{\{\mathbf{u} \in \Omega : u_i > \zeta_i\}} d\zeta_i \right) d\mathbf{x} \\ &= \int_0^1 \int_0^1 \int_{\Omega} (u - c_{11})^2 \mathbb{1}_{\{\mathbf{x} \in \Omega : u_1 > \zeta_1\}} \mathbb{1}_{\{\mathbf{x} \in \Omega : u_2 > \zeta_2\}} d\mathbf{x} d\zeta_1 d\zeta_2. \end{aligned}$$

Further similar computations yield,

$$\begin{aligned} \int_{\Omega} (u - c_{01})^2 (1 - u_1) u_2 d\mathbf{x} &= \\ &= \int_0^1 \int_0^1 \int_{\Omega} (u - c_{01})^2 (1 - \mathbb{1}_{\{\mathbf{x} \in \Omega : u_1 > \zeta_1\}}) \mathbb{1}_{\{\mathbf{x} \in \Omega : u_2 > \zeta_2\}} d\mathbf{x} d\zeta_1 d\zeta_2, \\ \int_{\Omega} (u - c_{10})^2 u_1 (1 - u_2) d\mathbf{x} &= \\ &= \int_0^1 \int_0^1 \int_{\Omega} (u - c_{10})^2 \mathbb{1}_{\{\mathbf{x} \in \Omega : u_1 > \zeta_1\}} (1 - \mathbb{1}_{\{\mathbf{x} \in \Omega : u_2 > \zeta_2\}}) d\mathbf{x} d\zeta_1 d\zeta_2, \\ \int_{\Omega} (u - c_{00})^2 (1 - u_1) (1 - u_2) d\mathbf{x} &= \\ &= \int_0^1 \int_0^1 \int_{\Omega} (u - c_{00})^2 (1 - \mathbb{1}_{\{\mathbf{x} \in \Omega : u_1 > \zeta_1\}}) (1 - \mathbb{1}_{\{\mathbf{x} \in \Omega : u_2 > \zeta_2\}}) d\mathbf{x} d\zeta_1 d\zeta_2. \end{aligned}$$

Defining $\mathbb{1}_{\mathbf{u}} := (\mathbb{1}_{\{\mathbf{x} \in \Omega : u_1 > \zeta_1\}}, \mathbb{1}_{\{\mathbf{x} \in \Omega : u_2 > \zeta_2\}})$, it follows that

$$\mathcal{G}(\mathbf{c}, \mathbf{u}) = \int_0^1 \int_0^1 \mathcal{G}(\mathbf{c}, \mathbb{1}_{\mathbf{u}}) d\zeta_1 d\zeta_2 = \int_0^1 \int_0^1 F(\mathbf{c}, \mathbf{u} - \boldsymbol{\zeta}) d\zeta_1 d\zeta_2,$$

for *a.e.* $\zeta = (\zeta_1, \zeta_2) \in [0, 1]^2$. Thus, it follows from the above equations that if \mathbf{u} is a minimizer of the convex relaxed problem (6), then for *a.e.* $\zeta \in [0, 1]^2$, the function $\mathbf{w}_1 = \mathbb{1}_{\mathbf{u}}$ is a minimizer of the problem (5). \square

Remark 1. Note also that $\mathbf{w}_2 = \mathbf{u} - \zeta$ is a solution of the original Vese and Chan minimization problem (1). This shows that the relaxed convex minimization problem is equivalent to the original Vese and Chan piecewise constant multiphase formulation (1), we refer to Chan et al [18] for more details.

The final segmentation is obtained by thresholding the functions u_1 and u_2 with any number in the interval $(0, 1)$ for example at 0.5, as shown in Figure 1(b) and (c). Note that the above modified minimization model does not involve level sets and thus can be solved efficiently. Further, we can prove that the above relaxed minimization problem can be solved in a binary variable minimization formulation to find a global minimum. The existence of minimizers of the modified energy \mathcal{G} given in Eqn. (6) is proved using the theory of functions of bounded variation (BV) space [28].

Theorem 2. For a given input gray scale image $I \in L^\infty(\Omega)$, there exists a minimizer for the functional \mathcal{G} in (6) in $\mathbb{R}^4 \times BV_{[0,1]}(\Omega)^2$.

Proof. Let $m := \inf \mathcal{G}(\mathbf{c}, \mathbf{u})$ and $\{(\mathbf{c}^k, \mathbf{u}^k)\}_{k=1}^\infty \subseteq \mathbb{R}^4 \times BV_{[0,1]}(\Omega)^2$ be a minimizer sequence for the energy \mathcal{G} , *i.e.*,

$$\mathcal{G}(\mathbf{c}^k, \mathbf{u}^k) \xrightarrow{k \rightarrow \infty} m.$$

Since $\{\mathbf{u}^k\}_{k=1}^\infty$ is bounded in $BV_{[0,1]}(\Omega)^2$, there is a subsequence also denoted by $\{\mathbf{u}^k\}_{k=1}^\infty$, strongly convergent to an element $\mathbf{u}^* \in L^1(\Omega)^2$. Furthermore, $\mathbf{u}^* \in L^1_{[0,1]}(\Omega)^2$. Therefore, it follows that $\mathbf{u}^* \in BV_{[0,1]}(\Omega)^2$ and

$$\int_{\Omega} |Du_i^*| \, d\mathbf{x} \leq \liminf_{k \rightarrow \infty} \int_{\Omega} |Du_i^k| \, d\mathbf{x} \quad (\text{with } i = 1, 2). \quad (7)$$

Now, considering \mathcal{G} as a function of \mathbf{c} , its minimization brings the following two equations,

$$\begin{aligned} c_{11}^k &= \frac{\int_{\Omega} I u_1^k u_2^k \, d\mathbf{x}}{\int_{\Omega} u_1^k u_2^k \, d\mathbf{x}}, & c_{10}^k &= \frac{\int_{\Omega} I u_1^k (1 - u_2^k) \, d\mathbf{x}}{\int_{\Omega} u_1^k (1 - u_2^k) \, d\mathbf{x}} \\ c_{01}^k &= \frac{\int_{\Omega} I (1 - u_1^k) u_2^k \, d\mathbf{x}}{\int_{\Omega} (1 - u_1^k) u_2^k \, d\mathbf{x}}, & c_{00}^k &= \frac{\int_{\Omega} I (1 - u_1^k) (1 - u_2^k) \, d\mathbf{x}}{\int_{\Omega} (1 - u_1^k) (1 - u_2^k) \, d\mathbf{x}}. \end{aligned}$$

Since $I \in L^\infty(\Omega)$, it follows $\{\mathbf{c}^k\}_{k=1}^\infty$ is uniformly bounded. Hence, there is a subsequence also denoted by $\{\mathbf{c}^k\}_{k=1}^\infty \subset \mathbb{R}^{2n}$ and a constant vector $\mathbf{c}^* \in \mathbb{R}^{2n}$ such that

$$\mathbf{c}^k \xrightarrow{k \rightarrow \infty} \mathbf{c}^*.$$

Then, from Fatou's lemma we get for the suitable sequence $\{(\mathbf{c}^k, \mathbf{u}^k)\}_{k=1}^\infty$:

$$\mathcal{G}(\mathbf{c}^*, \mathbf{u}^*) \leq \liminf_{k \rightarrow \infty} \mathcal{G}(\mathbf{c}^k, \mathbf{u}^k) = m,$$

i.e., $(\mathbf{c}^*, \mathbf{u}^*)$ is a minimizer of the functional \mathcal{G} . \square

Note that the \mathbf{c} values given in the above theorem are computed in the numerical scheme based on a dual minimization formulation which we describe next.

2.1 Implementation details

The four phase convex minimization problem in (6) is solved in an alternating fashion for the image variables (u_1, u_2) :

- First fix u_2 , and solve for u_1 :

$$\min_{u_1 \in [0,1]} \left\{ \mathcal{G}_1(u_1) = \int_{\Omega} |\nabla u_1| \, d\mathbf{x} + \int_{\Omega} r_1(\mathbf{c}, u_2) u_1 \, d\mathbf{x} \right\}.$$

- Then fix u_1 , and solve for u_2 :

$$\min_{u_2 \in [0,1]} \left\{ \mathcal{G}_2(u_2) = \int_{\Omega} |\nabla u_2| \, d\mathbf{x} + \int_{\Omega} r_2(\mathbf{c}, u_1) u_2 \, d\mathbf{x} \right\},$$

where the image region fitting terms are given by,

$$\begin{aligned} r_1(\mathbf{c}, u_2) &= (\lambda_{11}(I - c_{11})^2 - \lambda_{01}(I - c_{01})^2)u_2 \\ &\quad + (\lambda_{10}(I - c_{10})^2 - \lambda_{00}(I - c_{00})^2)(1 - u_2), \\ r_2(\mathbf{c}, u_1) &= (\lambda_{11}(I - c_{11})^2 - \lambda_{10}(I - c_{10})^2)u_1 \\ &\quad + (\lambda_{01}(I - c_{01})^2 - \lambda_{00}(I - c_{00})^2)(1 - u_1). \end{aligned}$$

To solve the above convex optimization problems we use the Chambolle's dual formulation [16, 12] of the total variation regularization function which occurs as the first term in the energy functional in Eqn. (6).

Thus, the new unconstrained minimization problems to consider are (for $j = 1, 2$):

$$\min_{u_j, v_j} \left\{ \int_{\Omega} |\nabla u_j| \, d\mathbf{x} + \frac{1}{2\theta_j} \|u_j - v_j\|_{L^2(\Omega)}^2 + \int_{\Omega} (r_j(\mathbf{c}, u_i)v_j + \alpha_j \nu(v_j)) \, d\mathbf{x} \right\},$$

where $j = 1, 2$ and $j \neq i$, θ_j is chosen to be small and $\nu(\xi) := \max\{0, 2|\xi - \frac{1}{2}| - 1\}$ and $\alpha_j > \frac{1}{2} \|r_j\|_{L^\infty(\Omega)}$.

We solve the above by further splitting into two sub-problems:

1. Solve for u_j :

$$\min_{u_j} \left\{ \int_{\Omega} |\nabla u_j| \, d\mathbf{x} + \frac{1}{2\theta_j} \|u_j - v_j\|_{L^2(\Omega)}^2 \right\}$$

The solution is given by

$$u_j = v_j - \theta_j \operatorname{div} \mathbf{p}_j.$$

The vector $\mathbf{p}_j = (p_{j_1}, p_{j_2})$ satisfy the equation

$$\nabla(\theta_j \operatorname{div} \mathbf{p}_j - v_j) - |\nabla(\theta_j \operatorname{div} \mathbf{p}_j - v_j)| \mathbf{p}_j = 0$$

and it is solve by a fixed point method: $\mathbf{p}_j^0 = 0$ and

$$\mathbf{p}_j^{n+1} = \frac{\mathbf{p}_j^n + \delta t \nabla(\text{div}(\mathbf{p}_j^n) - v_j/\theta_j)}{1 + \delta t |\nabla(\text{div}(\mathbf{p}_j^n) - v_j/\theta_j)|}.$$

2. Solve for the auxiliary variable v_j :

$$\min_{v_j} \left\{ \frac{1}{2\theta_j} \|u_j - v_j\|_{L^2(\Omega)}^2 + \int_{\Omega} (r_j(\mathbf{c}, u_i)v_j + \alpha_j \nu(v_j)) d\mathbf{x} \right\},$$

for which the solution is given by:

$$v_j = \min \{ \max(u_j(\mathbf{x}) - \theta_j r_j(\mathbf{c}, u_i), 0), 1 \}.$$

Furthermore, at every few iterations the vector \mathbf{c} is updated according to the following equations:

$$c_{11} = \frac{\int_{\Omega} I u_1 u_2 d\mathbf{x}}{\int_{\Omega} u_1 u_2 d\mathbf{x}}, \quad c_{10} = \frac{\int_{\Omega} I u_1 (1 - u_2) d\mathbf{x}}{\int_{\Omega} u_1 (1 - u_2) d\mathbf{x}}$$

$$c_{01} = \frac{\int_{\Omega} I (1 - u_1) u_2 d\mathbf{x}}{\int_{\Omega} (1 - u_1) u_2 d\mathbf{x}}, \quad c_{00} = \frac{\int_{\Omega} I (1 - u_1) (1 - u_2) d\mathbf{x}}{\int_{\Omega} (1 - u_1) (1 - u_2) d\mathbf{x}}.$$

The computation of \mathbf{c} values are similar to the ones in Vese and Chan model [48] (see Eqn. 1) except that they are now based on the binary partitioning functions and does not involve computing regularized Heaviside functions. We refer to [16] for more details on this particular form of dual minimization and the motivation for the fixed point method used to derive the solution for the auxiliary variable in the second step.

3 Experimental results

We have used full brain MRI images available at the whole brain atlas ¹. The parameters $\theta_1 = \theta_2 = 0.001$ were fixed for the segmentation results reported here. In order to simplify notations we use $\lambda = \lambda_{11} = \lambda_{01} = \lambda_{10} = \lambda_{00}$ and we fix $\lambda = 1$ in all our experiments as well. Equal weights are used for the four regions to be segmented as we do not want to introduce bias for certain phases. The images presented here are from $T1$ MRI imaging modality with slice thickness of $1mm$. Our scheme takes less than 0.2 seconds (for 100 iterations) on MATLAB2012a on a Mac laptop with Intel Core i7 CPU 2.3GHz, 8GB RAM CPU. Meanwhile, the average computation time for related models compared from the literature are in the region of 30 seconds (for 100 iterations) to converge to the final segmentation.

Figure 2 shows another example segmentation result of our globally convex four phase scheme. The noise (calculated relative to the brightest tissue, and denoted by "n") is set to 3% with intensity non-uniformity (denoted by "RF") is of strength 20%. The result of our four phase model is displayed in

¹<http://www.med.harvard.edu/aanlib/home.html>

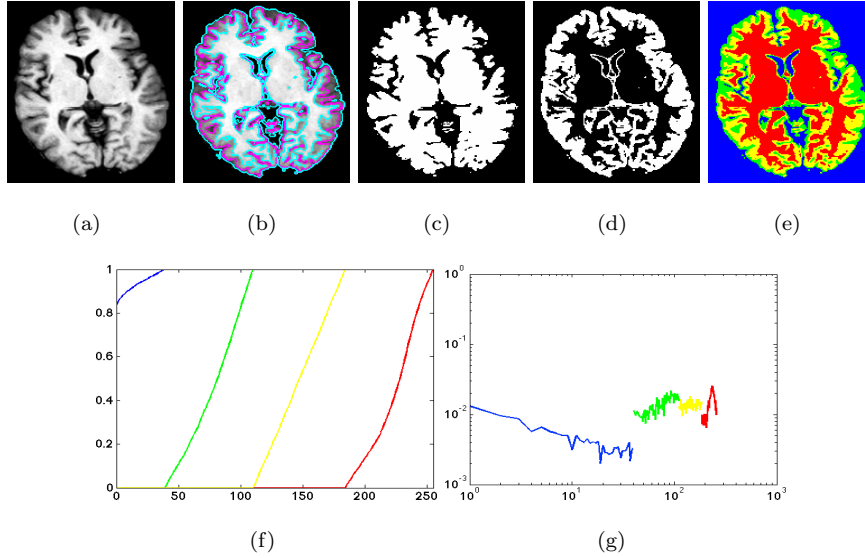


Figure 2: Our fast four phase image segmentation model provides good segmentation results by distinguishes the gray matter from the surrounding white. First row: (a) Input image. (b) Segmentation result with $\lambda = 1$. (c) Final binary segmentation u_1 . (d) Final binary segmentation u_2 . (e) Color visualization of the segmentation result. Second row: (f) Cumulative distribution function (CDF) of the four regions from (e). (g) Histogram of the four regions showing the separation clearly.

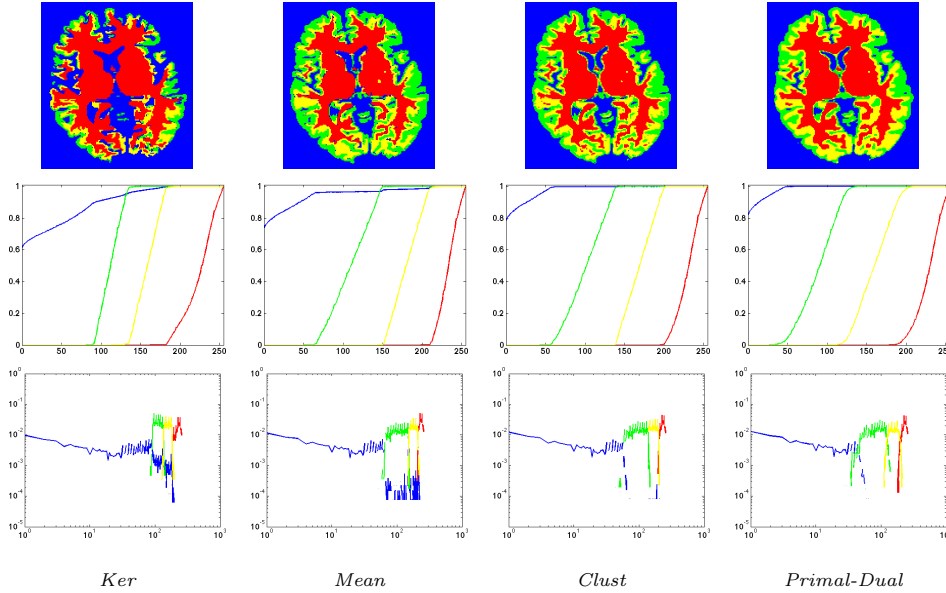


Figure 3: Comparison with *Ker*, *Mean*, *Cluster*, *Mean*, *Primal-Dual* multiphase segmentation methods. First row: Color coded visualization of the obtained segmentation result. Second row: Cumulative distribution function (CDF) of the four computed regions. Third row: Histogram of the four regions showing the intersections.

Figure 2(b) with two contours (Purple, Light-Blue) overlaid on top of the input image. Figure 2(c) and (d) show the two functions u_1, u_2 computed using our scheme and thresholded at 0.5. The function u_1 captures the background shape 2(a) (corresponding to level set ϕ_1) whereas function u_2 in Figure 2(b) (corresponding to level set ϕ_2) contains the white matter. Figure 2(e) we use four different colors (Blue, Green, Yellow, and Maroon) to highlight different phases for better visualization of phase separation and boundary detection of regions. In Figure 2(f) and (g), we show cumulative distribution function (CDF) and the histogram of each of the four regions computed by the proposed method. The histograms highlight separation of different phases/regions indicating the superior performance of our splitting based numerical approach.

Figure 3 shows a comparison result with other multiphase active contour methods from [5, 7, 10, 17] called in short, Ker, Mean, Clust and Primal-Dual respectively, for the same image in Figure 2(a). Note that to make a fair comparison with other models we used the same noise level and intensity non-uniformity for this example image. In Figure 3 bottom two rows we show the cumulative distribution function (CDF) and histograms computed for each of the computed phases respectively. Compared with the histograms shown in Figure 2(f) and (g) for our scheme we see that proposed model provides better separation of regions. The histograms for the other schemes in Figure 3 (last row) show nontrivial intersections, highlighting the drawback in using level set based implementations. Moreover, the noise remains as speckles in the segmented regions whereas our model handles it efficiently.

3.1 Error metrics computation

We use the following quantitative error metrics to compare the schemes with gold standard ground truth segmentations. For more details about objective evaluation of image segmentation algorithms and for precise definitions of these metrics we refer to [47].

- **DICE:**

The Dice coefficient [22] is a popular error metric and is used to compare ground truth segmentation with those obtained with automatic multiphase segmentation schemes. By definition, for two binary segmentations A and B , the Dice coefficient is computed as:

$$D(A, B) = \frac{2|A \cap B|}{|A| + |B|}. \quad (8)$$

Here the binary segmentation is computed automatically, using the segmentation curves and by thresholding regions obtained by all algorithms. The notation $|A|$ denotes the number of pixels in the set A . Note that, a D value of 1 indicates perfect agreement. In particular, higher numbers indicate that the results of that particular scheme's result match the gold standard better than results that produce lower Dice coefficients.

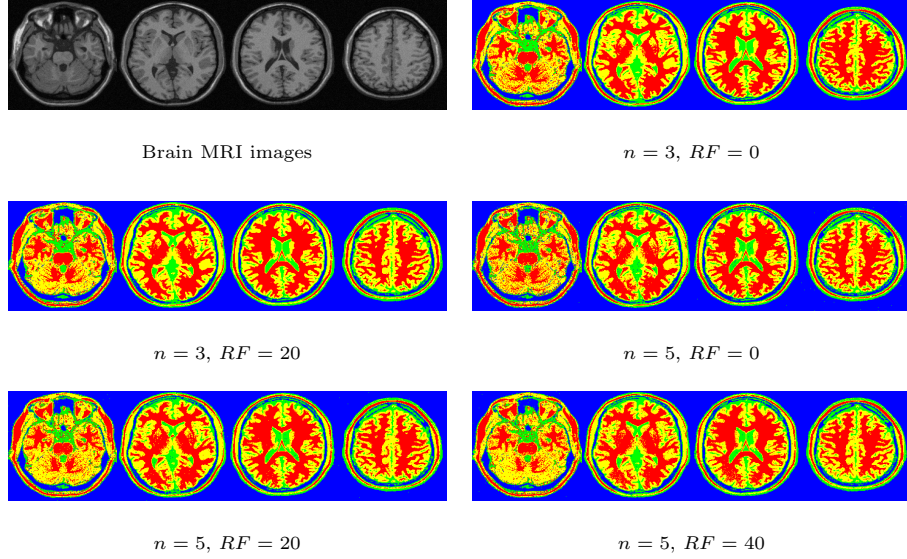


Figure 4: Segmentation results for full Brain data-sets with representative axial slices. First (top-left) subfigure shows the noise-free brain MRI images. Next subfigures present segmentation results for different noise (“ n ”) and non-uniformity (“ RF ”) values for our scheme. Segmentation results are stable for increasing values of noise and intensity inhomogeneities.

- **RI:**

Rand Index: A metric based on a classical nonparametric test and is computed by counting pairs of pixels that have compatible label relationships in the two segmentations to be compared.

- **GCE:**

Global Consistency Error: A metric which computes the degree of overlap of the cluster associated with each pixel in one segmentation and its closest approximation in the other segmentation. Values to closer to 0 indicate better segmentation results.

- **VI:**

Variation of Information: A metric related to the conditional entropies between the class label distribution of the segmentations. This computes a measure of information content in each of the segmentations and how much information one segmentation gives about the other. Values closer to 1 indicate better segmentation results.

Note that all these metrics are for comparing two segmentations, one of which is assumed to be the available ground truth. Table 1 shows the comparison of average Dice values (for 181 images) of different models for different noise and intensity inhomogeneities taken from Brainweb database. As can be seen our scheme performs better in terms of the Dice coefficient compared with other related approaches. Similarly in Table 2 we see that the average RI, GCE and VI for different schemes against our model

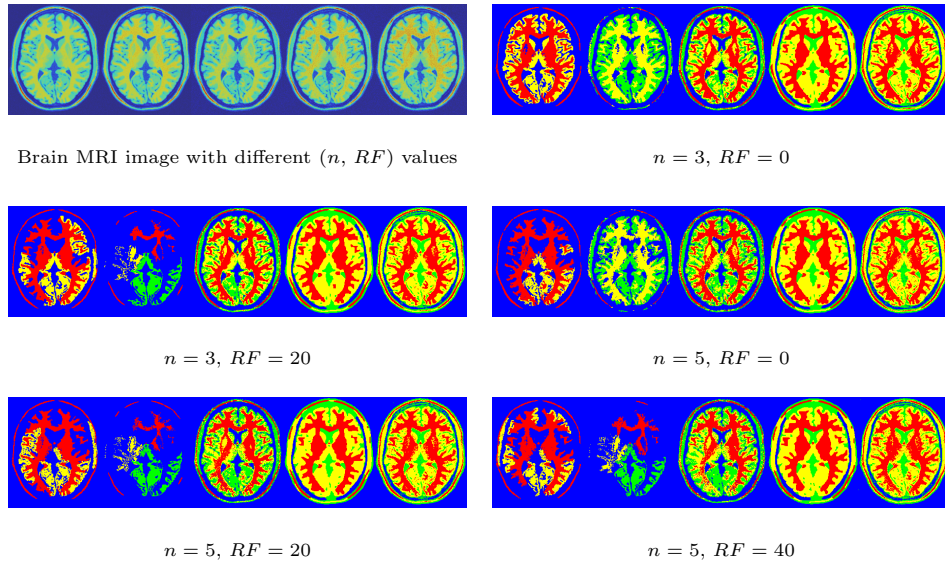


Figure 5: Comparison of color segmentation visualization for a single brain MRI image (Slice number 79) with different (n, RF) levels. The top-left subfigure is different input images. Remaining subfigures contain different segmentation results. From left to right: Ker, Mean, Clust, Primal-dual, and Our approach, respectively.

shows that the proposed globally convex multiphase scheme performs well overall.

Figure 4 shows representative segmentation results for full Brain data-sets (axial slices are shown) with different noise (“ n ”) and non-uniformity (“ RF ”) levels for our scheme. Different n and RF are specified in Figure 4 for each row. This illustrates that our scheme preserves the topological changes as we move through the image stack. Moreover, our scheme can handle noise and intensity non-uniformity together effectively. Finally, in Figure 5 we show different segmentation results for a particular image (slice number 79) taken across all noise and inhomogeneity levels for different schemes. The results indicate that Ker and Mean methods can lead to poor separation of different regions whereas noise can affect the result of Clust and Primal-Dual schemes. Meanwhile, our approach performs well and handles higher non-uniformity without degrading the final segmentation results. Further data-sets and extensive comparison results of all the schemes for full brain stacks are available online ².

4 Conclusion

We study a fast globally convex four phase active contour scheme for MRI image segmentation and provide a well posed convex energy minimization which can be used to determine piecewise constant segmentation without level sets. By using a dual minimization based implementation our approach provides better

²<http://dx.doi.org/10.6084/m9.figshare.781297>

Table 1: Average Dice coefficients values for different schemes in four different phases. Values near 1 indicate the closeness of the segmentation to the ground truth segmentation. Best results are indicated by boldface.

n	RF	Regions	Ker	$Mean$	$Clust$	$Primal-Dual$	Our
3	0	D1	0.305670	0.824283	0.886665	0.698128	0.944007
		D2	0.224586	0.581326	0.419365	0.700223	0.915818
		D3	0.131252	0.363182	0.110626	0.718244	0.870375
		D4	0.565510	0.840712	0.693652	0.955584	0.965933
3	20	D1	0.306836	0.767452	0.873386	0.692621	0.931111
		D2	0.223917	0.534288	0.432176	0.695534	0.907063
		D3	0.130171	0.303436	0.110716	0.718225	0.873175
		D4	0.563268	0.823805	0.645526	0.953754	0.967594
5	0	D1	0.305627	0.788663	0.877971	0.688774	0.912402
		D2	0.226171	0.539260	0.311053	0.680036	0.879323
		D3	0.126738	0.299720	0.100588	0.688052	0.829607
		D4	0.544178	0.807202	0.669333	0.948687	0.954868
5	20	D1	0.309830	0.746360	0.866684	0.708890	0.903028
		D2	0.225578	0.510120	0.318350	0.685553	0.870886
		D3	0.132034	0.253848	0.111433	0.683057	0.824065
		D4	0.539861	0.780266	0.613947	0.944511	0.953657
5	40	D1	0.310085	0.715360	0.825330	0.685356	0.872111
		D2	0.226430	0.478908	0.286386	0.678544	0.844355
		D3	0.130849	0.221841	0.127278	0.670710	0.806790
		D4	0.542354	0.766757	0.586870	0.543010	0.951143

Table 2: Average Rand Index (RI), Global Consistency Error (GCE) and Variation of Information (VI) for for different schemes. Best results are indicated by boldface.

n	RF	Error Metrics	Ker	$Mean$	$Clust$	$Primal-Dual$	Our
3	0	RI	0.527025	0.849013	0.672026	0.895372	0.946341
		GCE	0.332322	0.223942	0.158767	0.173467	0.085668
		VI	2.483764	1.177137	1.490298	0.992642	0.569099
3	20	RI	0.525251	0.833570	0.659371	0.887008	0.941475
		GCE	0.329012	0.236016	0.171285	0.189292	0.096797
		VI	2.477927	1.255048	1.564992	1.065011	0.620833
5	0	RI	0.523815	0.825506	0.648725	0.884315	0.921506
		GCE	0.333999	0.250001	0.154166	0.194308	0.135605
		VI	2.507981	1.326232	1.563033	1.087131	0.828043
5	20	RI	0.522536	0.813937	0.629603	0.877183	0.917244
		GCE	0.330010	0.252157	0.166120	0.209219	0.142290
		VI	2.495524	1.375133	1.642941	1.148695	0.858660
5	40	RI	0.520192	0.805794	0.604564	0.865636	0.905678
		GCE	0.326658	0.256492	0.176804	0.231084	0.163501
		VI	2.489061	1.423080	1.737919	1.240130	0.950309

phase differentiation than other schemes. Experimental results on brain MRI images indicate the proposed approach provides better results compared with other active contour based multiphase segmentation schemes.

Vector valued version similar to [19] is straightforward and our current implementation can handle RGB color images as well. Currently we are developing a three dimensional version for obtaining surface segmentations from MRI images similar to [24] as well as a method to extract intensity non-uniformity patterns coupled with segmentations [52].

References

- [1] Mohamed N. Ahmed, Sameh M. Yamany, Nevin Mohamed, Aly A. Farag, and Thomas Moriarty. A modified fuzzy c-means algorithm for bias field estimation and segmentation of MRI data. *Medical Imaging, IEEE Transactions on*, 21(3):193–199, 2002.
- [2] Umberto Amato, Michele Larobina, Anestis Antoniadis, Bruno Alfano, et al. Segmentation of magnetic resonance brain images through discriminant analysis. *Journal of neuroscience methods*, 131(1-2):65–74, 2003.
- [3] M. Stella Atkins and Blair T. Mackiewicz. Fully automatic segmentation of the brain in MRI. *Medical Imaging, IEEE Transactions on*, 17(1):98–107, 1998.
- [4] H. Attouch, G. Buttazzo, and G. Michaille. *Variational analysis in Sobolev and BV spaces: Applications to PDEs and optimization*. Society for Industrial and Applied Mathematics (SIAM), Philadelphia, PA, USA, 2006.
- [5] I. Ben Ayed and A. Mitiche. A partition constrained minimization scheme for efficient multiphase level set image segmentation. In *ICIP*, pages 1641–1644, 2006.
- [6] I. Ben Ayed and A. Mitiche. A region merging prior for variational level set image segmentation. *IEEE Trans. Image Process.*, 17(12):2301–2311, 2008.
- [7] I. Ben Ayed, A. Mitiche, and Z. Belhadj. Polarimetric image segmentation via maximum likelihood approximation and efficient multiphase level sets. *IEEE Trans. Pattern Anal. Mach. Intell.*, 28(9):1493–1500, 2006.
- [8] E. Bae, J. Yuan, and X.-C. Tai. Global minimization for continuous multiphase partitioning problems using a dual approach. *International Journal of Computer Vision*, 92(1):112–129, 2011.
- [9] Mohd Ali Balafar, AR Ramli, M Iqbal Saripan, and Syamsiah Mashohor. Review of brain MRI image segmentation methods. *Artificial Intelligence Review*, 33(3):261–274, 2010.

- [10] M. Ben Salah, A. Mitiche, and I. Ben Ayed. Effective level set image segmentation with a kernel induced data term. *IEEE Transactions on Image Processing*, 19(1):220–232, 2010.
- [11] James C Bezdek, LO Hall, and L.P Clarke. Review of MR image segmentation techniques using pattern recognition. *Medical physics*, 20:1033, 1993.
- [12] X. Bresson, S. Esedoglu, P. Vanderghenst, J. Thiran, and S. Osher. Fast global minimization of the active contour/snake model. *Journal of Mathematical Imaging and Vision*, 28(2):151–167, 2007.
- [13] E. Brown, T. F. Chan, and X. Bresson. A convex relation method for a class of vector-valued minimization problems with applications to Mumford-Shah segmentation. Technical Report 43, UCLA CAM, 2010.
- [14] E. S. Brown, T. F. Chan, and X. Bresson. Completely convex formulation of the Chan-Vese image segmentation model. *International Journal of Computer Vision*, 98(1):103–121, 2012.
- [15] F. A.M. Cappabianco, A. X. Falcao, C. L. Yasuda, and J. K. Udupa. Brain tissue mr-image segmentation via optimum-path forest clustering. *Computer Vision and Image Understanding*, 116(10):1047 – 1059, 2012.
- [16] A. Chambolle. An algorithm for total variation minimization and applications. *Journal of Mathematical Imaging and Vision*, 20(1–2):89–97, 2004.
- [17] A. Chambolle and T. Pock. A first-order primal-dual algorithm for convex problems with applications to imaging. *Journal of Mathematical Imaging and Vision*, 40(1):120–145, 2011.
- [18] T. F. Chan, S. Esedoglu, and M. Nikolova. Algorithms for finding global minimizers of image segmentation and denoising models. *SIAM Journal on Applied Mathematics*, 66(5):1632–1648, 2006.
- [19] T. F. Chan, B. Y. Sandberg, and L. A. Vese. Active contours without edges for vector-valued images. *Journal of Visual Communication and Image Representation*, 11(2):130–141, 2000.
- [20] T. F. Chan and L. A. Vese. Active contours without edges. *IEEE Transactions on Image Processing*, 10(2):266–277, 2001.
- [21] Keh-Shih Chuang, Hong-Long Tzeng, Sharon Chen, Jay Wu, and Tzong-Jer Chen. Fuzzy c-means clustering with spatial information for image segmentation. *computerized medical imaging and graphics*, 30(1):9–15, 2006.
- [22] L. R. Dice. Measures of the amount of ecologic association between species. *Ecology*, 26(3):297–302, 1945.

- [23] G. Dogan, P. Morin, and R. H. Nochetto. A variational shape optimization approach for image segmentation with a mumford-shah functional. *SIAM Journal on Scientific Computing*, 30(6):3028–3049, 2008.
- [24] C. S. Drapaca, V. Cardenas, and C. Studholme. Segmentation of tissue boundary evolution from brain MR image sequences using multi-phase level sets. *Computer Vision and Image Understanding*, 100(3):312–329, 2005.
- [25] I. N. Figueiredo, J. C. Moreno, and V. B. S. Prasath. Texture image segmentation with smooth gradients and local information. In *Computational Modeling of Objects Presented in Images: Fundamentals, Methods and Applications (CompIMAGE 2012)*, pages 164–171, Rome, Italy, September 2012.
- [26] I. N. Figueiredo, J. C. Moreno, V. B. S. Prasath, and P. N. Figueiredo. A segmentation model and application to endoscopic images. In *International Conference on Image Analysis and Recognition (ICIAR 2012)*, pages 164–171, Aveiro, Portugal, June 2012. Springer LNCS Volume 7325 (eds.: A. Campilho and M. Kamel).
- [27] Bruce Fischl, David H Salat, Evelina Busa, Marilyn Albert, Megan Dieterich, Christian Haselgrove, Andre van der Kouwe, Ron Killiany, David Kennedy, Shuna Klaveness, et al. Whole brain segmentation: automated labeling of neuroanatomical structures in the human brain. *Neuron*, 33(3):341–355, 2002.
- [28] F. Giusti. *Minimal Surfaces and Functions of Bounded Variation*. Birkhauser, Basel, Switzerland, 1984.
- [29] Laura Gui, R. Lisowski, T. Faundez, and P. S. Huppi. Automatic segmentation of newborn brain mri using mathematical morphology. In *ISBI*, pages 2026–2030, Chicago, IL, USA, 2011.
- [30] S. H. Kang and R. March. Existence and regularity of minimizers of a functional for unsupervised multiphase segmentation. *Nonlinear Analysis: Theory, Methods & Applications*, 76:181–201, 2013.
- [31] M. S. Keegan, B. Sandberg, and T. F. Chan. A multiphase logic framework for multichannel image segmentation. *Inverse Problems and Imaging*, 6(1):95–110, 2012.
- [32] J. Koh, P. D. Scott, V. Chaudhary, and G. Dhillon. An automatic segmentation method of the spinal canal from clinical mr images based on an attention model and an active contour model. In *ISBI*, pages 1467–1471, Chicago, IL, USA, 2011.
- [33] C. Li, C.-Y. Kao, J. C. Gore, and Z. Ding. Minimization of region-scalable fitting energy for image segmentation. *IEEE Transactions on Image Processing*, 17(10):1940–1949, 2008.

- [34] Liang Liao, Tusheng Lin, and Bi Li. MRI brain image segmentation and bias field correction based on fast spatially constrained kernel clustering approach. *Pattern Recognition Letters*, 29(10):1580–1588, 2008.
- [35] Alan Wee-Chung Liew and Hong Yan. An adaptive spatial fuzzy clustering algorithm for 3-D MR image segmentation. *Medical Imaging, IEEE Transactions on*, 22(9):1063–1075, 2003.
- [36] Z. Ma, J. M. R. S. Tavares, R. N. M. Jorge, and T. Mascarenhas. A review of algorithms for medical image segmentation and their applications to the female pelvic cavity. *Computer Methods in Biomechanics and Biomedical Engineering*, 13(2):235–246, 2010.
- [37] Jose L. Marroquin, Baba C. Vemuri, Salvador Botello, E Calderon, and Antonio Fernandez-Bouzas. An accurate and efficient bayesian method for automatic segmentation of brain MRI. *Medical Imaging, IEEE Transactions on*, 21(8):934–945, 2002.
- [38] S. Merino-Caviedes, G. Vegas-Sanchez, M.T. Perez, S. Aja-Fernandez, and M. Martin-Fernandez. Automatic segmentation of newborn brain MRI using mathematical morphology. In *ISBI*, pages 908–911, Rotterdam, 2010.
- [39] J. C. Moreno. *Contributions to Variational Image Segmentation*. PhD thesis, University of Coimbra, Portugal, September 2012.
- [40] D. Mumford and J. Shah. Optimal approximations by piecewise smooth functions and associated variational problems. *Communications in Pure and Applied Mathematics*, 42(5):577–685, 1989.
- [41] S. Osher and J. A. Sethian. Fronts propagating with curvature-dependent speed: algorithms based on Hamilton-Jacobi formulations. *Journal of Computational Physics*, 79(1):12–49, 1988.
- [42] Nikhil R Pal and Sankar K Pal. A review on image segmentation techniques. *Pattern recognition*, 26(9):1277–1294, 1993.
- [43] Dzung L Pham, Chenyang Xu, and Jerry L Prince. Current methods in medical image segmentation. *Annual review of biomedical engineering*, 2(1):315–337, 2000.
- [44] V. B. S. Prasath, F. Bunyak, P. S. Dale, S. R. Frazier, and K. Palaniappan. Segmentation of breast cancer tissue microarrays for computer-aided diagnosis in pathology. In *First IEEE Healthcare Technology Conference: Translational Engineering in Health & Medicine*, Houston, TX, USA, November 2012.
- [45] V. B. S. Prasath, K. Palaniappan, and G. Seetharaman. Multichannel texture image segmentation using weighted feature fitting based variational active contours. In *Eighth Indian Conference on Vision, Graphics and Image Processing (ICVGIP)*, pages 78:1–78:6, Mumbai, India, December 2012.

- [46] Shan Shen, William Sandham, Malcolm Granat, and Annette Sterr. MRI fuzzy segmentation of brain tissue using neighborhood attraction with neural-network optimization. *Information Technology in Biomedicine, IEEE Transactions on*, 9(3):459–467, 2005.
- [47] R. Unnikrishnan, C. Pantofaru, and M. Hebert. Toward objective evaluation of image segmentation algorithms. *IEEE Transactions on Pattern Analysis and Machine Intelligence*, 29(6):929–944, 2007.
- [48] L. Vese and T. F. Chan. A multiphase level set framework for image segmentation using the Mumford and Shah model. *International Journal of Computer Vision*, 50(3):271–293, 2002.
- [49] WM Wells III, W Eric L Grimson, Ron Kikinis, and Ferenc A Jolesz. Adaptive segmentation of MRI data. *Medical Imaging, IEEE Transactions on*, 15(4):429–442, 1996.
- [50] Nan Zhang, Su Ruan, S. Lebonvallet, Qingmin Liao, and Yuemin Zhu. Kernel feature selection to fuse multi-spectral MRI images for brain tumor segmentation. *Computer Vision and Image Understanding*, 115(2):256 – 269, 2011.
- [51] Yongyue Zhang, Michael Brady, and Stephen Smith. Segmentation of brain MR images through a hidden markov random field model and the expectation-maximization algorithm. *Medical Imaging, IEEE Transactions on*, 20(1):45–57, 2001.
- [52] Ying Zhuge and Jayaram K. Udupa. Intensity standardization simplifies brain MR image segmentation. *Computer Vision and Image Understanding*, 113(10):1095 – 1103, 2009.